

Modelling Thickness-Dependence of Ferroelectric Thin Film Properties

L. Pálová, P. Chandra, and K.M. Rabe

Center for Materials Theory, Department of Physics and Astronomy, Rutgers University, Piscataway, NJ 08854

We present a segregated strain model that can describe the thickness-dependent dielectric properties of epitaxial ferroelectric films. Using a phenomenological Landau approach, we present results for two specific materials, making comparison with experiment and with first-principles calculations whenever possible. We also suggest a “smoking gun” benchtop probe to test our model.

I. INTRODUCTION

Increasing demands for high-density data storage with ultra-fast accessibility present tremendous challenges. In parallel to the characterization of new materials, important size-dependent effects must be understood to optimize design. This is particularly true for ferroelectric memories, whose nonvolatility and low power consumption make them well-suited for portable applications;^{1,2} their dielectric properties are strongly dependent on electromechanical boundary conditions due to the long-range nature of their underlying electrostatic interactions. The sensitivity of ferroelectricity to homogeneous strain in bulk perovskite oxides is well-known.³ In thin films, the effects of homogeneous misfit strain have been identified,⁴ studied and controlled to the point that particular systems have been strain-engineered to have spontaneous polarizations significantly larger than those in the bulk.^{5,6} Despite these impressive achievements, several authors^{7,8,9,10} have suggested that homogenous epitaxial strain cannot qualitatively account for all the observed effects in ferroelectric films. In particular, the thickness-dependence of their dielectric properties has been attributed to defect-induced strain gradients.^{7,9} In this paper we explore whether these observed size-effects are also consistent with an alternative scenario where the majority of each ferroelectric film is homogeneously strained. Our phenomenological study indicates that thickness-dependent dielectric measurements are insufficient to determine the presence/absence of underlying inhomogeneous strain and we suggest further benchtop experiments that will resolve this issue.

In well-screened coherent epitaxial ferroelectric thin films, uniform polarization is energetically favored. Lattice mismatch between the film and the substrate is a key source of macroscopic strain in these systems.^{4,11} For very thin films, the energy cost for homogeneously straining the film to match the substrate is less than that associated with the introduction of stress-relieving defect structures at the interface. However in thicker films, such misfit dislocations form and produce strain gradients^{7,11,12,13,14}; threading dislocations and point defects are additional sources of inhomogeneous strain. In planar ferroelectric films, inhomogeneous strain can affect the ferroelectric transition through both smearing and through its coupling to the polarization. Such flexoelectric coupling of strain gradients to the polarization has been the topic of much recent interest^{9,15,16} particularly

as it has been suggested that flexoelectric effects are enhanced by large dielectric coefficients.¹⁷ Recently it has been argued that such strain/stress gradients are crucial for the modelling of thickness-dependent dielectric properties of ferroelectric films.^{7,9} Here we propose an alternative model: that the misfit dislocations reside within a thin buffer layer next to the interface; the majority of the film, which is relatively defect-free, is then homogeneously strained.¹⁸ In our phenomenological treatment, we also include a bulk anisotropy¹⁰ in the form of an effective field,¹⁹ possibly due to asymmetry of the electrodes and/or to the thin buffer layer. We model the thickness-dependent dielectric properties in two different types of ferroelectric films, and compare our results with experiment and with first-principles calculations whenever possible. Finally we discuss a benchtop “smoking gun” probe to distinguish our segregated strain scenario with that of inhomogeneous strain in ferroelectric thin films.

The structure of this paper is as follows. In Section II we review the experiments that motivate this study and their implications for any descriptive model. Details of our phenomenological Landau approach are presented in Section III, with specific discussion of the appropriate boundary conditions and depolarization effects. In Section IV we present our main results for films of two specific materials, with comparison to previous findings whenever possible and predictions for future measurements. The implications of our model and our results are discussed in Section V. We end with a summary (Section VI) and with ideas for future work.

II. EXPERIMENTAL MOTIVATION

Broadening of the temperature-dependent permittivity in thin films near the paraelectric-ferroelectric transition is reported by several experimental groups;^{20,21,22,23,24} this observed smearing, accompanied by an overall reduction in its magnitude, is more pronounced with decreasing film thickness. Careful measurements on free-standing ferroelectric lamellae yield bulk-type dielectric responses, suggesting interfacial effects as the source of these thickness-dependent effects.²⁵ A second related observation is that there is a clear separation of temperature scales associated with the onset of reversible spontaneous polarization and the maximum of the dielectric constant in thin ferroelectric films.⁹

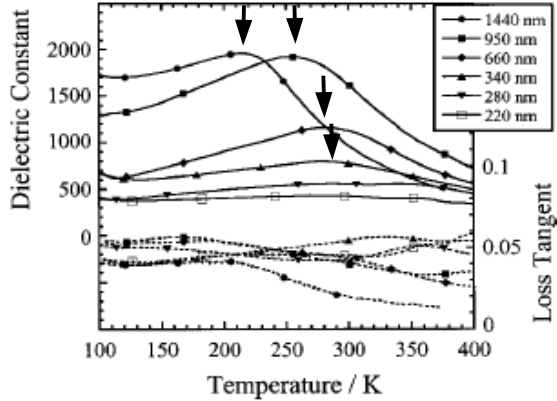


Figure 1: Relative permittivity (dielectric constant) as a function of temperature ($\epsilon(T)$) for $(Ba, Sr)TiO_3$ (BST) films of different thicknesses grown on $SrRuO_3/MgO$ (SRO) substrates²³ where the $\epsilon_{max}(T)$ at temperature T_{max} is indicated with an arrow.

In Fig. 1 we display relative permittivity measurements done on $(Ba, Sr)TiO_3$ (BST) thin films grown on $SrRuO_3$ (SRO).²³ The measurements show suppression of the relative permittivity with decreasing film thickness. As the film thickness decreases to 340 nm, the temperature associated with the maximum of the permittivity (T_{max}) appears to saturate at about 300 K, with T_{max} for the two thinnest films not being clearly discernable. As we will discuss in Section IV, this is consistent with the prediction of our model that there should be a maximum in $T_{max}(l)$ at a thickness $l = l^*$; from the data in Figure 1 we estimate $l^* < 340$ nm in BST films grown on SRO.

In ferroelectric films, in contrast with their bulk counterparts, there is an observed distinction⁹ between T_{max} and T_{ferro} , the temperature where polarization becomes switchable. This separation of temperature-scales and the permittivity broadening discussed earlier are both features characteristic of dielectric behavior in an applied bias field¹⁹; the latter could be due to a real charge distribution or it could result from another physical effect¹⁰ that breaks the symmetry $P \rightarrow -P$. For example it has been noted⁹ that flexoelectric coupling, known to increase near a ferroelectric transition,¹⁵ implies a spatially-varying effective field term due to the underlying inhomogeneous strain⁹. The resulting phenomenological model successfully reproduces key thickness-dependences of the dielectric properties.⁹ Here we ask whether these experimental trends are indeed proof of underlying strain inhomogeneities, or whether they may be consistent with another strain profile.

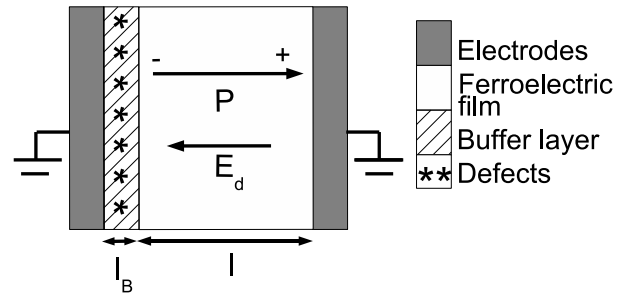


Figure 2: A schematic of the planar ferroelectric capacitor under consideration, with the key length-scales and regions clearly demarcated. Note that the mismatch defects are segregated in a buffer layer of thickness l_B and that the polarization and strain are homogeneous in the majority of the film. Incomplete charge compensation at the ferroelectric-electrode interfaces results in a residual depolarization field, as shown.

Segregated Strain Model

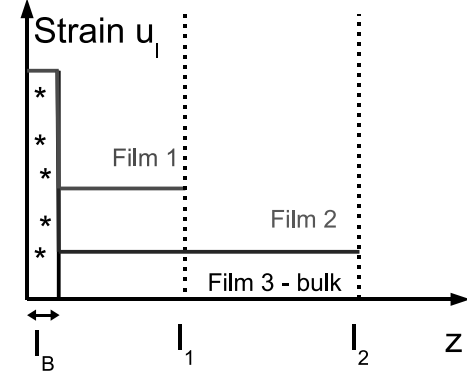


Figure 3: Schematic of the segregated strain model; here the elastic defects reside within l_B ($\ll l$) of the film-substrate interface so that the majority of the film is homogeneously strained.

III. LANDAU THEORY

We model the thickness-dependent properties of strained ferroelectric films using a Landau approach^{3,26} where all misfit dislocations are assumed to reside within a thin buffer layer of size $l_B \ll l$ where l is the film thickness (e.g. Fig. 2); this is in contrast to other approaches where these defects are assumed to be roughly uniformly distributed within the film.⁷ Elastic relaxation then occurs so that there is homogeneous strain in the film except for the buffer layer (e.g. Fig. 3). Recent X-ray diffraction experiments²³ support previous suggestions²⁷ that the in-plane film strain, u_l , decreases with increasing thickness (l) of the overall films; furthermore the observed thickness-dependent strain fits an exponential

form^{23,27} very well. Therefore in our segregated strain approach, thin films experience homogeneous film strain that decreases exponentially with their overall thickness l ; more specifically we model this thickness-dependent in-plane film strain as

$$u_l = u_m e^{-l/l_c}, \quad u_m = (b - a)/b, \quad (1)$$

where l_c is a characteristic length-scale of the strain relaxation, and a and b refer to the in-plane lattice parameters of the film (bulk value) and the substrate, respectively¹⁸. We emphasize that our values of l_c are determined from X-ray diffraction^{23,27} for films of a range of thicknesses. We note that these values of l_c are comparable to the film thicknesses of interest ($l_c \sim l$), resulting in a non-trivial thickness-dependence of the strain-related properties. More generally, we remark that the segregated strain approach described here has been used in modelling epitaxially strained superlattices²⁸ with results that are consistent with experiment.²⁹

In Fig. 2 we display a schematic of the planar ferroelectric capacitor under consideration with the length-scales involved. More specifically we assume a single-domain ferroelectric film with the (uniaxial) polarization in the z -direction, normal to the film-substrate interface. Physically we expect a build-up of free surface charge at the ferroelectric boundaries which, if uncompensated, results in a depolarization field E_d . In practice such depolarization effects are significantly reduced by metal electrodes that provide charge compensation; however their non-ideal nature means that some residual depolarization field remains. Because E_d is proportional to $\frac{l}{l_e}$, where l_e is the screening length of the electrodes, its importance increases with reduced film thickness^{11,26,30,31} and becomes significant^{32,33} for $l \sim 100\text{nm}$; a term in our Landau expansion will be included to account for these depolarization effects.

The defect buffer layer is also displayed in Fig. 2 and, as discussed above, we assume homogeneous (but possibly relaxed relative to the substrate) strain in the remainder of the ferroelectric film which is controlled by the substrate-film lattice mismatch. Following a previous analysis of epitaxially strained films,⁴ the stress tensors $\sigma_{zz} = \sigma_{xz} = \sigma_{yz} = 0$, because there are no tractions acting on the top film surface. For the special case of a (001) ferroelectric film grown on a cubic substrate, the strain $u_{xx} = u_{yy} = u_l$ and $u_{xy} = 0$ since the angle between the two lattice vectors remains unchanged ($\theta = \frac{\pi}{2}$). We consider here film tetragonal symmetry with $u_{zz} \neq 0$ and $u_{yz} = u_{xz} = 0$. These mixed mechanical boundary conditions associated with two-dimensional clamping mean that the standard elastic free energy $G(P, \sigma)$ cannot be used to find the equilibrium properties of these systems; instead a Legendre transformation, $G'(P, u_l) = G(P, \sigma) + u_l(\sigma_{xx} + \sigma_{yy}) + u_{zz}\sigma_{zz}$, to a modified thermodynamic potential must be performed in order to study the equilibrium properties of the constrained film.⁴

We are almost ready to write an expression for

$G'(P, u_l)$ and to calculate observable thermodynamic quantities. As discussed earlier, the experiments suggest a term in G that breaks the symmetry $P \rightarrow -P$; this is achieved by linear coupling of P to an external electric field E_{ext} and/or to an effective bias field¹⁰ which we take to be of the form

$$W_l = W_0 e^{-l/l_w}, \quad (2)$$

where $l_w \sim l_c$. We note that the thickness-dependence of W_l is included to model the increased smearing of the dielectric susceptibility with decreasing l of ferroelectric films.¹⁰ At present we will treat W_l phenomenologically, and will defer discussion of its exponential decay and its possible origins to Section V.

Putting all these elements together, we begin our phenomenological study with the free-energy expansion

$$\begin{aligned} G(P, \bar{\sigma}, T) = & \frac{1}{2}\tilde{\alpha}(T)P^2 + \frac{1}{4}\gamma P^4 - (W_l + E_{ext})P \\ & - Q_{11}\sigma_{zz}P^2 - Q_{12}(\sigma_{xx} + \sigma_{yy})P^2 \\ & - \frac{1}{2}s_{11}(\sigma_{xx}^2 + \sigma_{yy}^2 + \sigma_{zz}^2) - s_{12}(\sigma_{xx}\sigma_{yy}) \\ & - s_{12}\sigma_{zz}(\sigma_{xx} + \sigma_{yy}) - \frac{1}{2}s_{44}\sigma_{xy}^2, \end{aligned} \quad (3)$$

where $\tilde{\alpha}(T) = \alpha(T) + \alpha_d$; $\alpha(T) = \beta(T - T_{bulk})$, T_{bulk} is the bulk transition temperature, α_d is discussed below, and β and γ are Landau coefficients; here Q_{ij} and s_{ij} are the electrostrictive constants and the elastic compliances at constant polarization respectively. The depolarization field contributes to the free energy through the coefficient $\tilde{\alpha}(T)$ in Eq.(3)^{26,34}

$$\alpha_d = \frac{l_e}{\epsilon_0 \epsilon_e l}, \quad (4)$$

where l_e is the screening length of the electrodes, and ϵ_0 and ϵ_e are the electric permittivities of the vacuum and the electrodes respectively.

The mechanical conditions in the film are $\partial G / \partial \sigma_{xx} = \partial G / \partial \sigma_{yy} = -u_l$, $\partial G / \partial \sigma_{xy} = 0$ and $\partial G / \partial \sigma_{zz} = -u_{zz}$ ⁴. Solving for the in-plane stresses, one finds that $\sigma_{xy} = 0$ and $\sigma_{xx} = \sigma_{yy} \equiv \sigma$, where the applied in-plane stress σ is eliminated by the in-plane strain $u_l(\sigma)$. This procedure, together with $\sigma_{zz} = 0$, leads to

$$\begin{aligned} G'(P_l, u_l, T) = & \frac{u_l^2}{s_{11} + s_{12}} + \frac{1}{2}\alpha_l^*(T)P_l^2 \\ & + \frac{1}{4}\gamma^*P_l^4 - (W_l + E_{ext})P_l, \end{aligned} \quad (5)$$

where $\gamma^* = \gamma + \frac{4Q_{12}^2}{s_{11} + s_{12}}$ and $\alpha_l^*(T) = \alpha(T) - u_l \frac{4Q_{12}}{s_{11} + s_{12}} + \alpha_d$. We note that we explicitly refer to the l -dependence of the polarization (P_l), which here results from the thickness-dependence of the strain (u_l), the bias field (W_l) and depolarization field term (α_d), consistent with observation.⁹ One can express the out-of-plane strain

(u_{zz}) through its dependence on the out-of-plane polarization (P_l) and the in-plane strain (u_l) as

$$u_{zz}(P_l, u_l) = \frac{2s_{12}}{s_{11} + s_{12}} u_l + \left(Q_{11} - \frac{2s_{12}}{s_{11} + s_{12}} Q_{12} \right) P_l^2. \quad (6)$$

The Curie film temperature T_c^* refers to the paraelectric-ferroelectric transition at zero total field, $E_l^T \equiv W_l + E_{ext} = 0$. It increases with an applied compressive strain ($Q_{12} < 0$)

$$T_c^* = T_{bulk} + \frac{1}{\beta} \left[u_l \frac{4Q_{12}}{s_{11} + s_{12}} - \frac{l_e}{\epsilon_0 \epsilon_e l} \right] \quad (7)$$

but has a decreasing component for very thin films due to depolarization effects. The dielectric susceptibility is

$$\chi_l^{-1} = \epsilon_0 \frac{d^2 G}{dP_l^2} = \epsilon_0 \left[\alpha_l^*(T) + 3\gamma^* P_l^2 \right] \quad (8)$$

which diverges at T_c^* if the spontaneous polarization $P_l \rightarrow 0$; that can only occur if $E_l^T = 0$ (see Eq. 10 below). The dielectric susceptibility is observed to diverge for bulk systems³ and for free-standing films.²⁵ In general $E_l^T \neq 0$ for ferroelectric capacitors and $P_l \neq 0$ at T_c^* , so that χ_l has a finite maximum at a temperature T_{max} defined by $\frac{\partial \chi_l}{\partial T}|_{T=T_{max}} = 0$. We note that this condition combined with the expression for χ_l above yields

$$P_l(T) \frac{dP_l(T)}{dT} \Big|_{T_{max}} = -\frac{\beta}{6\gamma^*} \quad (9)$$

where we see that T_{max}^l differs from T_c^* and depends on film thickness via the polarization; this equation generally has to be solved numerically to obtain T_{max}^l once the expression for $P_l(T)$ has been determined.

The condition for finding the system in its equilibrium state is $\frac{\partial G}{\partial P} = 0$. The spontaneous polarization P_l emerges then as the solution(s) to the following cubic equation

$$\alpha_l^*(T) P_l + \gamma^* P_l^3 = E_l^T \quad (10)$$

where for $E_l^T = W_l + E_{ext} \neq 0$, we have to be careful to distinguish between the paraelectric (nonswitchable) polarization P_p and the ferroelectric (switchable) polarization P_f ; here switchable refers to the fact that there are multiple solutions for the polarization that can be accessed by application of a finite E_{ext} . There are three solutions to the equation (10)

$$P_p = \left(\frac{E_l^T}{2\gamma^*} + \sqrt{\mathcal{R}} \right)^{1/3} - \left(-\frac{E_l^T}{2\gamma^*} + \sqrt{\mathcal{R}} \right)^{1/3} \quad (11)$$

and

$$P_f = \frac{1}{2} P_p \pm i \frac{\sqrt{3}}{3} \left(\left(\frac{E_l^T}{2\gamma^*} + \sqrt{\mathcal{R}} \right)^{1/3} + \left(-\frac{E_l^T}{2\gamma^*} + \sqrt{\mathcal{R}} \right)^{1/3} \right), \quad (12)$$

Table I: Landau parameters for $BST^{4,9}$ and STO^{37} (in SI units). We use the $T > 100K$ values for $\alpha(T)$, except in calculations in Fig. 15 where we interpolate the $T > 100K$ and the $T < 50K$ values to $75K$ where the two $\alpha(T)$ functions cross.

film	$\gamma(T) [10^6]$	Q_{11}	Q_{12}	$s_{11} + s_{12} [10^{-12}]$
BST	$4(796 + 2.16(T - 273))$	0.110	-0.0430	5.6
STO	1700	0.066	-0.0135	3.0
film	$\alpha(T) [10^5]$			
BST	$9.1(T - 235.0)$			
STO ($T > 100K$)	$7.06(T - 35.5)$			
STO ($T < 50K$)	$263.5 (\text{Coth}[42.0/T] - 0.90476)$			

Table II: Film parameters: effective field W_0 and compressive strain $u_m^{6,9}$ with associated length-scales l_w and l_c^{23} (see Eqs. 1 and 2); also the values for screening length l_e^{36} and the relative permittivity ϵ_e of electrodes are shown.

film	substrate	$W_0 [kV/cm]$	$l_w [\text{nm}]$	$u_m [\%]$	$l_c [\text{nm}]$	$l_e [\text{nm}]$	ϵ_e
BST	SRO	400	300	-0.50	300	0.023	1.0
BST	PSS	450	300	-0.77	300	0.400	1.0
STO	LSAT	400	300	-0.90	300	0.023	1.0

where

$$\mathcal{R} \equiv \frac{\alpha_l^{*3}(T)}{27\gamma^{*3}} + \frac{(E_l^T)^2}{4\gamma^{*2}} \quad (13)$$

and the number of polarization solutions is determined by the sign of \mathcal{R} so that the single nonswitchable P_p corresponds to $\mathcal{R} > 0$. Therefore the transition temperature T_{ferro} between nonswitchable and switchable polarization occurs when $\mathcal{R} = 0$ leading to the expression

$$T_{ferro} = T_c^* - \frac{3}{\beta} \left(\frac{\gamma^*}{4} \right)^{1/3} (E_l^T)^{2/3}. \quad (14)$$

At this temperature, the paraelectric solution becomes an unstable extremum.

In general, the three temperature-scales T_{ferro} , T_{max} and T_c^* differ as indicated in Fig. 4. We note that for very thin films (< 60 nm), there is suppression of all three temperatures due to depolarization effects. We also remark on the presence of a maximum in $T_{max}(l)$ that has already been alluded to in Section II; this feature will be discussed in more detail when we apply this phenomenology to specific materials and substrates.

IV. RESULTS

In this section, we calculate dielectric properties for two specific materials, $(Ba_{0.5}Sr_{0.5})TiO_3$ (BST) and $SrTiO_3$ (STO). Our study of BST films allows us to make direct comparison between our calculated properties and

the experiments (Fig. 1) that motivated the inhomogeneous strain scenario.⁹ In order to explore different parameter regimes, we study these films on two distinct substrates, $SrRuO_3$ (SRO) and $Pt/SiO_2/Si$ (PSS); here we note that the latter is a hypothetical case since to date epitaxially-grown single-crystal films of BST on PSS have not yet been realized.

We also apply our phenomenological treatment to STO films that are known for their coherence; this is achieved by highly controlled growth conditions that inhibit defect formation and thus inhomogeneous strain effects are not expected.⁶ To our knowledge, there do not exist published high-resolution dielectric measurements of strained STO films with polarization normal to the electrode-ferroelectric interface. We therefore compare our results whenever possible to first-principles calculations,³⁵ and make experimental predictions for a range of epitaxial strain values that could be realized by a variety of substrates.

The parameters used in our calculations are presented in Tables I and II. Table I indicates the Landau coefficients used for each material. Film-related parameters, displayed in Table II, are determined from data on strain relaxation; the characteristic length l_c (see Eq. 1) from the lattice constant measurements lies somewhere between 200 and 300 nm^{23,27}. In order to make comparison with the inhomogeneous strain model scenario, which uses a characteristic length scale 300 nm⁹, we keep this l_c value in our calculations. Data on electrode screening lengths (l_e) is l_e of $SrRuO_3$ (SRO) 0.23 Å³⁶, and we set l_e of $(LaAlO_3)_{0.29} \times (SrAl_{0.5}Ta_{0.5}O_3)_{0.71}$ (LSAT) to be the same value, since LSAT is dominated by $SrAl_{0.5}Ta_{0.5}O_3$ that is very similar to SRO. We choose the screening length of $Pt/SiO_2/Si$ (PSS) to be $l_e = 4$ Å, which is expected to be larger than l_e in metallic SRO due to the presence of semiconducting silicon. We display strain u_m value for three different substrates, BST on SRO,⁹ BST on PSS ($a_{BST} = 3.95$ Å, $b_{Pt} = 3.92$ Å) and STO on LSAT.⁶ The bias field is set to be $W_0 = 4.0 \times 10^7$ V/m for BST films on SRO, a value that is comparable to that of applied external fields in related BST dielectric measurements.²³ We keep the same W_0 for STO films and a slightly different one ($W_0 = 4.5 \times 10^7$ V/m) for BST films on PSS. The bias field W_l is treated phenomenologically (see Eq. 2) and we emphasize its crucial role in modelling key features of the dielectric properties of ferroelectric films as will be discussed in more detail shortly.

A. BST

In Fig. 4 we display the three temperature-scales as a function of thickness for BST films on SRO electrodes with $E_{ext} = 0$: T_{max} , T_c^* and T_{ferro} . Because $E_l^T = W_l \neq 0$, there is a clear separation of the three temperatures; for $E_l^T = 0$, they collapse onto T_c^* (compare Eqs. 7, 9 and 14). Therefore an estimate of W_0 can be obtained from the difference of T_{max} and T_c^* , where

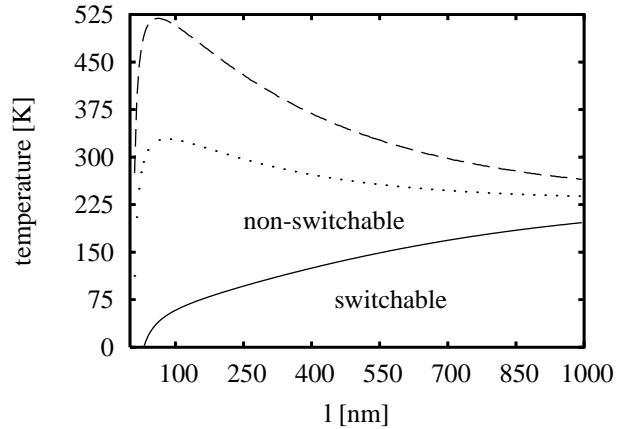


Figure 4: Thickness-dependence of the three distinct temperature-scales T_{ferro} (solid), T_{max} (dashed) and T_c^* (dotted line) with $E_{ext} = 0$ in the segregated defect model described in the text; here Landau coefficients for BST on SRO (see Tables I and II in Section IV) have been used and $T_{max}(l)$ is noted to display a peak at $l^* = 60$ nm.

the latter can be expressed in terms of (experimentally accessible) Landau parameters and by the value of the misfit strain (Eq. 7). The magnitude of the obtained bias field, $W_0 = 400$ kV/cm, is in rough agreement with experiment: the experimental temperature $T_{max}^{exp} = 250$ K for a 950 nm film in Fig. 1 is close to the calculated $T_{max}^{calc} = 268$ K in Fig. 4 and $T_{max}^{exp} = 280$ K for the 660 nm film in Fig. 1 is also reasonably close to the calculated $T_{max}^{calc} = 304$ K in Fig. 4.

The temperature T_{max} displays a peak, $T_{max} = 519$ K at $l^* = 60$ nm, and it decreases with increasing thickness and asymptotically approaches T_c^* , the bulk transition temperature. As previously noted in Section II, for $l < l^*$, T_{max} decreases with decreasing l ; by contrast for $l > l^*$, the trend is consistent with that displayed in Fig. 1. More generally, the behavior of T_{max} depends on that of the polarization as a function of temperature (see Eq. 9). Both the strain and the bias field make the polarization decrease with increasing film thickness ($l > 60$ nm) as will be discussed shortly, and this monotonic behavior makes T_{max} decrease as well. The observed peak in T_{max} is driven by the depolarization field contribution in our model. T_{max} becomes suppressed for very thin films ($l < 60$ nm) and approaches zero just as does the polarization at these film thicknesses (see Fig. 7). The value of $l^* = 60$ nm is determined by the strength of the depolarization contribution, and thus is expected to depend on the electrode/substrate material. As already noted, we use a longer l_e for BST films on PSS than for BST on SRO. Because the depolarization field contribution to our free energy is proportional to $\frac{l_e}{l}$, (see Eq. 4), the resulting l^* will be larger for BST on PSS than on the SRO substrate. For BST on PSS, we calculate that the peak in T_{max} occurs at $l^* \sim 300$ nm in contrast to the value of $l^* \sim 60$ nm for BST on SRO displayed in

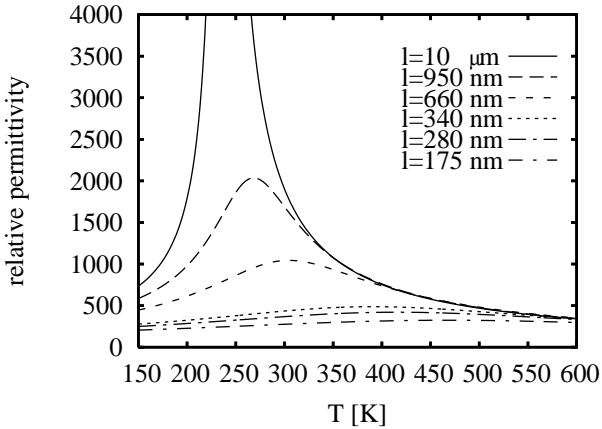


Figure 5: Calculated relative permittivity as a function of temperature for *BST* films on *SRO* substrates of thicknesses $l = 10\mu\text{m}$, 950, 660, 340, 280 and 175 nm with $E_{ext} = 0$. The highest permittivity corresponds to the thickest film; the divergence for $10\mu\text{m}$ film at the bulk Curie temperature 235 K is indicated. Reduction in the permittivity for thin films is observed; the peak of the permittivity shifts towards higher temperatures in agreement with Fig. 1.

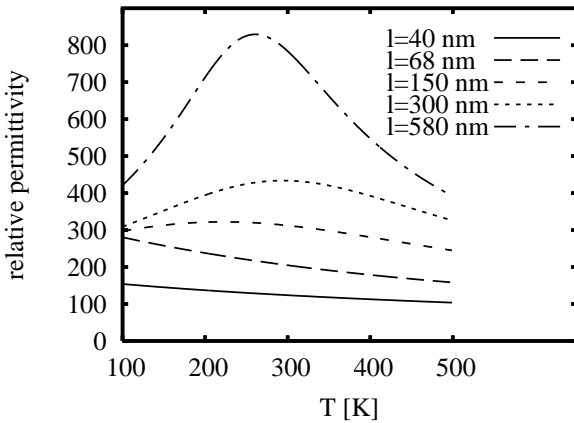


Figure 6: Calculated relative permittivity as a function of temperature for *BST* films epitaxially grown on *PSS* substrates of thicknesses $l = 40, 68, 150, 300$ and 580 nm with $E_{ext} = 0$. The highest permittivity corresponds to the thickest film. Reduction in the permittivity for thin films is observed, and the peak of permittivity shifts towards lower temperatures.

Fig. 4.

The theoretical temperature T_c^* in Fig. 4 refers to the paraelectric-ferroelectric transition at zero total field, $E_l^T = W_l + E_{ext} = 0$ (see Eq. 7). It has a peak at 80 nm with a maximum value of $T_c^* = 329$ K and then decreases with increasing film thickness due to the strain relaxation term, $u_l \sim e^{-l/l_c}$. It reaches its bulk transition temperature value ($T_{bulk} = 235$ K) for thicker fully relaxed films: $T_c^* = 238$ K for 1000 nm film. Due to the depolarization contribution (see Eq. 4), T_c^* is suppressed for very thin films and eventually reaches zero.

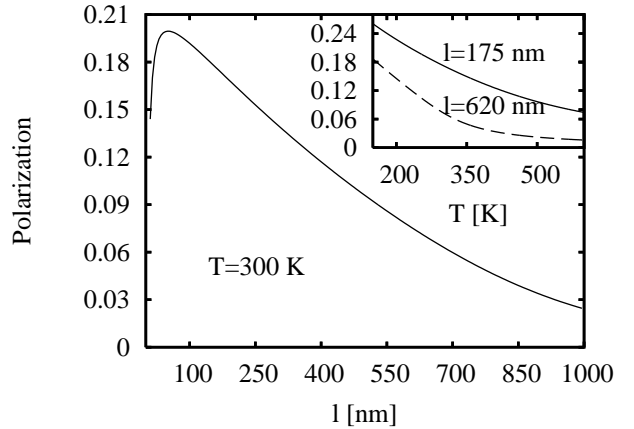


Figure 7: Calculated nonswitchable polarization $P[\frac{C}{m^2}]$ (see Fig. 4) for *BST* films on *SRO* substrates of various thicknesses (l) at temperature 300 K and with $E_{ext} = 0$; polarization as a function of temperature for films of thickness 175 nm (solid) and 620 nm (dashed line) are shown in the inset.

The temperature T_{ferro} that separates switchable and nonswitchable polarization regimes increases for increasing l and saturates when it reaches the bulk transition temperature. In Eq. 14 we see that there is competition between thickness-dependent contributions due to u_l and to W_l in T_{ferro} ; therefore whether this temperature increases or decreases with increasing film thickness depends on their relative magnitudes. For example, T_{ferro} is shown to increase with increasing l in Figure 4, reflecting the dominance of the bias field contribution in this particular case. We note that the switchable (ferroelectric) regime is lost as the films become very thin: e.g. ferroelectricity vanishes at $l \sim 100$ nm at fixed temperature 60 K. T_{ferro} reaches zero at a critical film thickness ($l_{crit} \sim 35$ nm here) and films with $l < l_{crit}$ remain in the nonswitchable polarization regime at all temperatures.

In Fig. 5 we display our calculated relative permittivity $\epsilon(T)$ ($\epsilon = 1 + \chi$) for *BST* films on *SRO* substrates with $E_{ext} = 0$. Reduction in $\epsilon(l)$ as a function of decreasing thickness is observed for both theory and experiment (Fig. 1); ϵ_{max} decreases and T_{max} increases as l decreases. Favorable comparison of the calculated relative permittivity ϵ_{max}^{calc} can be made to its measured analog²³ ϵ_{max}^{exp} shown in Fig. 1: $\epsilon_{max}^{calc} = 2035$ at $T_{max} = 268$ K matches with $\epsilon_{max}^{exp} \approx 1900$ at $T_{max} \approx 260$ K for the 950 nm film, and $\epsilon_{max}^{calc} = 1044$ at $T_{max} = 304$ K matches with the $\epsilon_{max}^{exp} \approx 1100$ at $T_{max} \approx 290$ K for the 660 nm film.

We also predict the thickness-dependent dielectric behavior of $\epsilon(T)$ for *BST* films epitaxially grown on *PSS* in Fig. 6. For films of decreasing thickness where $l < l^*$ a systematic reduction in ϵ is observed and the peak in the permittivity is shifted to lower temperatures.

Next we present the calculated nonswitchable polarization in Fig. 7 at temperature 300 K with $E_{ext} = 0$ for *BST* films on *SRO*. The polarization is roughly proportional to the bias field W_l and its value increases with

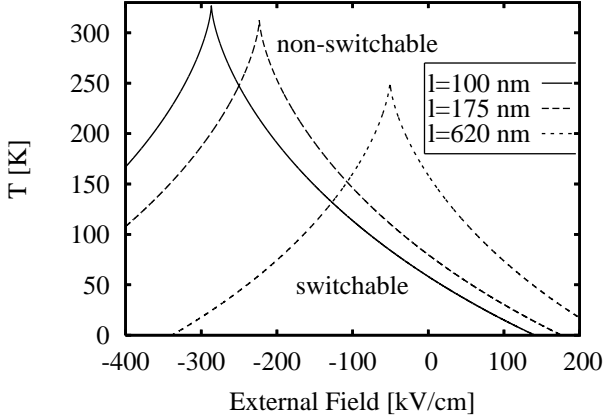


Figure 8: Transition temperature T_{ferro} as a function of applied external electric field E_{ext} for *BST* films on *SRO* substrates of thicknesses 100 (solid), 175 (dashed) and 620 nm (dotted line). The corresponding line divides the region into switchable and nonswitchable polarization phases for each film.

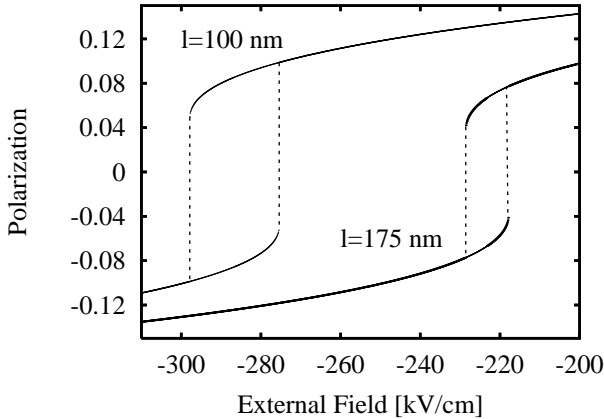


Figure 9: Calculated hysteresis polarization loops for *BST* films on *SRO* substrates of thicknesses 100 and 175 nm at temperature 290 K.

increasing misfit strain u_l (see Eq. 10). Motivated by experiment, we have modelled the bias field and misfit strain to decrease with increasing film thickness exponentially ($\{W_l, u_l\} \sim e^{-l/l_x}$, $l_x = \{l_w, l_c\}$), and therefore the polarization also decreases with thicker films. However, for very thin films ($l < 50$ nm), there is suppression of the polarization (P) due to depolarization field effects and a peak with a maximum value of polarization $P_{max} = 0.2$ [C/m^2] at $l = 50$ nm develops. The temperature-dependence of the polarization for two different film thicknesses is displayed in the inset of Fig. 7. These $P(T)$ curves shows good qualitative agreement with analogous measurements.⁹ In general, the polarization decreases with increasing temperature.

T_{ferro} , the transition temperature separating the presence of switchable and nonswitchable spontaneous polar-

ization, is plotted in the presence of external electric field for *BST* films on *SRO* in Fig. 8. $T_{ferro}(E_{ext})$ reaches its maximum at $E_{ext} = -W_l$ (where $W_l = W_0 e^{-l/l_c}$), and decreases symmetrically about this value in agreement with Eq. 14; we note that the maximum of T_{ferro} decreases for thicker films as anticipated by the zero-total field (E_l^T) results of T_c^* displayed in Fig. 4. The temperature T_{ferro} at zero external field matches the behavior of Fig. 4. Switchable and nonswitchable polarization phases are marked.

Calculated hysteresis loops are displayed in Fig. 9 for *BST* films on *SRO* substrates at $T = 290$ K with $l = 100$ nm and $l = 175$ nm. According to Fig. 8, at this temperature for these film thicknesses, the switchable polarization develops only for certain values of nonzero external electric field: $E_{ext} = \{-298, -275\}$ kV/cm for 100 nm film and $E_{ext} = \{-229, -218\}$ kV/cm for 175 nm film. The width of the hysteresis loops in Fig. 9 is given by the above field ranges; it decreases with increasing film thickness and shows good qualitative agreement with experiment.²³ Hysteresis loops are symmetric around the point $E_{ext} = -W_l$ and $P = 0$, where the bias field W_l is the thickness-dependent field offset. This field offset (specifically, we refer to the shift of the center of the hysteresis loop along the field axis from zero field position) becomes larger for thinner films (see Eq. 2) and is temperature independent. However, the width of the loops shrinks as temperature is increased, as shown in Fig. 8. Symmetry in the hysteresis loops around $P = 0$ yields zero offset in the spontaneous polarization and therefore no associated charge offset within the thin film. We note that significant charge offsets are observed in graded films with designed polarization and strain gradients.⁴²

B. Strained STO

Bulk strontium titanate $SrTiO_3$ (STO) remains paraelectric down to the lowest temperatures accessible, but strained STO films may be driven into a ferroelectric phase even at room temperature.⁶ To our knowledge, detailed thickness-dependent dielectric measurements on such STO films have been performed only with tensile epitaxial strain resulting to in-plane polarization.^{6,38} Here we make predictions for the thickness-dependent dielectric properties of STO films with compressive epitaxial strains and polarizations normal to the film-substrate interface.

We begin by making direct comparison between our results and those of ab-initio studies,³⁵ displayed in Figs. 10,11. Since ab-initio calculations consider uniformly strained films without strain relaxation and without an effective bias field, we set $W_l = 0$ for the purpose of comparison here. In Fig. 10 we present the spontaneous polarization as a function of misfit strain for a $l = 100$ nm STO film at zero total field, $E_l^T = 0$. Dots in the figure correspond to first-principles calculations,³⁵ where the out-of-plane polarization in the ferro-

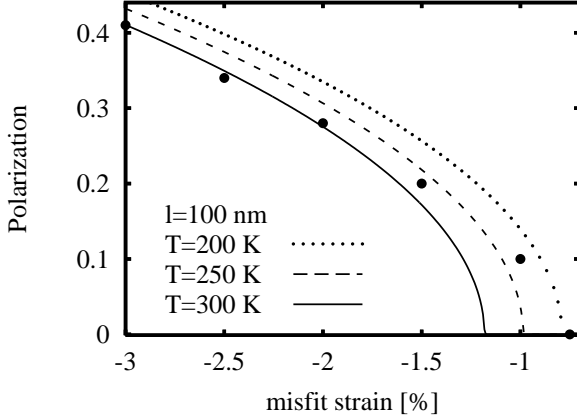


Figure 10: Spontaneous polarization $P[C/m^2]$ as a function of film strain (u_l) for 100 nm STO film at temperatures $T = 200$ (dotted), $T = 250$ (dashed) and $T = 300$ K (solid line) and zero total field, $E_l^T = 0$. Dots correspond to ab-initio values of the polarization³⁵.

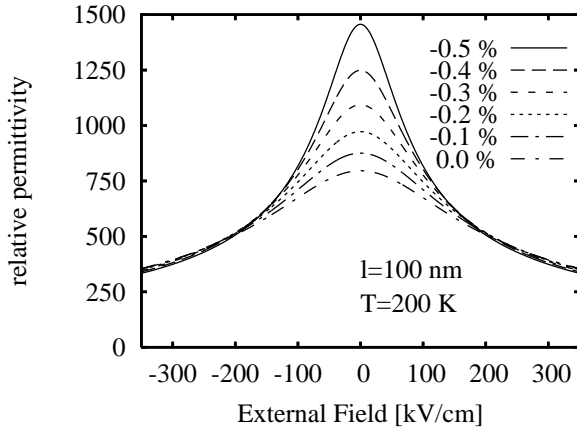


Figure 11: Calculated paraelectric relative permittivity as a function of external electric field E_{ext} and film strain $u_l = -0.5, -0.4, -0.3, -0.2, -0.1$ and 0.0% for 100 nm STO film at temperature $T = 200$ K. The permittivity data are shown in the limit of zero bias field W_l in order to make comparison with the ab-initio data³⁵.

electric tetragonal phase ($u_l < -0.75\%$) for films with zero macroscopic field has been calculated. We choose the $l = 100$ nm STO film where we do not expect depolarization effects to be important ($l > l^*$; see Fig. 14) for comparison with the ab-initio data. Good agreement is achieved at temperatures $T \sim 250$ K; our calculated curves follow the behavior of the ab-initio dots. At lower temperatures, better agreement is achieved for less compressive strain, correctly indicating that fully relaxed STO is paraelectric down to zero temperature.

Continuing our comparison with the results of ab-initio calculations,³⁵ we display the paraelectric relative permittivity as a function of external electric field E_{ext} and film strain u_l for a $l = 100$ nm STO film at $T = 200$ K in Fig. 11. A nonpolar tetragonal phase develops for

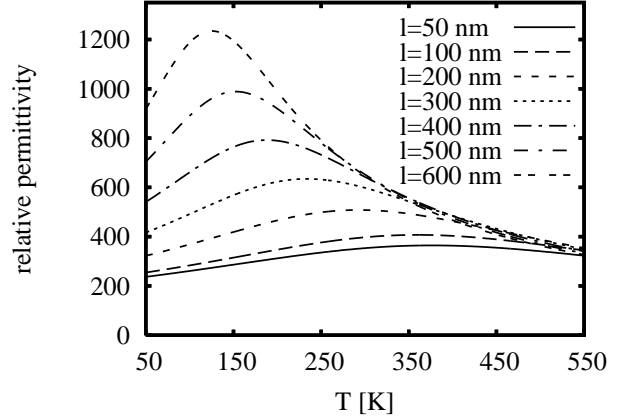


Figure 12: Calculated relative permittivity as a function of temperature for STO films of thicknesses $l = 50, 100, 200, 300, 400, 500$ and 600 nm at misfit compressive strain $u_m = -0.9\%$ with $E_{ext} = 0$. The highest permittivity corresponds to the thickest film. Reduction in the permittivity for thin films is observed.

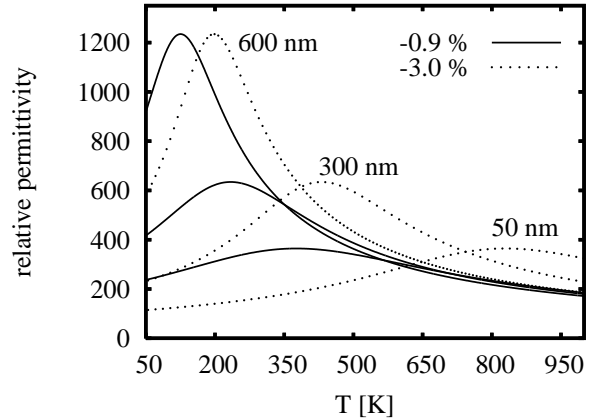


Figure 13: Calculated relative permittivity as a function of temperature for STO films of thicknesses $l = 50, 300$ and 600 nm at misfit strain $u_m = -0.9\%$ (solid) and $u_m = -3.0\%$ (dotted) with $E_{ext} = 0$. Higher values of misfit compressive strain shifts the permittivity curve towards higher temperatures where the larger shifts of T_{max} are observed for the thinner films.

strains $-0.75\% < u_l < +0.54\%$ according to the ab-initio calculations.³⁵ From Fig. 10, the best fit for the polarization just at the paraelectric-ferroelectric phase boundary ($u_l = -0.75\%$) is achieved at $T = 200$ K, and therefore we choose this temperature to calculate our paraelectric permittivity data. We compare our results to the ab-initio calculations in the range of compressive strain $-0.5\% < u_l < 0.0\%$: in both cases, the permittivity (ϵ) increases with increasing compressive strain; this occurs even more rapidly in the range of external fields $-150 < E_{ext} < 150$ kV/cm, and its magnitude in the range $800 \leq \epsilon \leq 1500$ in Fig. 11 roughly corresponds to the ab-initio values $400 \leq \epsilon \leq 1800$.³⁵ We note that the

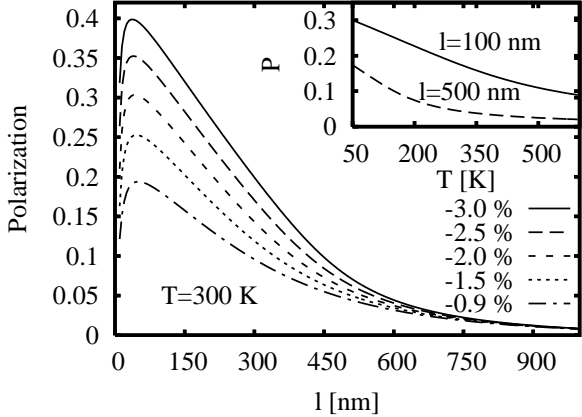


Figure 14: Calculated nonswitchable polarization $P [C/m^2]$ of STO films as a function of film thickness (l) for misfit strains $u_m = -3.0, -2.5, -2.0, -1.5$ and -0.9% at temperature 300 K and with $E_{ext} = 0$. In the inset, the polarization as a function of temperature (T) is plotted for 100 (solid) and 500 nm (dashed line) films at misfit strain $u_m = -0.9\%$ and zero external field.

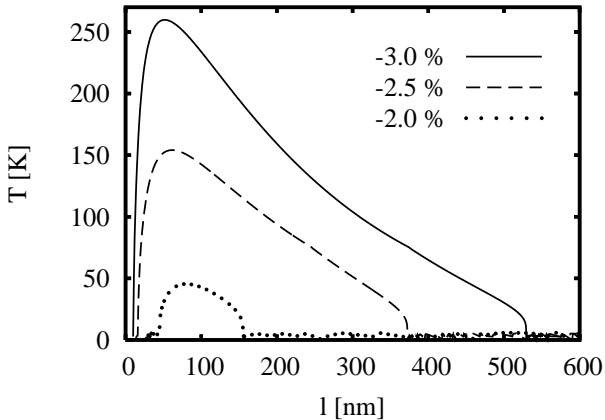


Figure 15: Transition temperature T_{ferro} separating switchable (below) and nonswitchable (above the temperature curve) polarization phases as a function of STO film thickness l and misfit strain $u_m = -3.0, -2.5$ and -2.0% with $E_{ext} = 0$. T_{ferro} becomes negative for compressive misfit strain values smaller than 1.5% for all film thicknesses, resulting in a nonswitchable polarization regime.

observed increase of the paraelectric permittivity with strain can be understood from Eq. 8.

Both Figs. 10 and 11 indicate good agreement between results of our phenomenological model and those of previous first-principles calculations, and this provides us with confidence regarding the Landau coefficients and more generally with the approach described here applied to strained STO films. Next we calculate the dielectric properties of strained STO films using a nonzero value for the effective bias field, $W_0 = 400$ kV/cm, that is comparable to that used for BST films in Sec IV A.

Our calculated relative permittivity as a function of

temperature and film thickness at compressive strain $u_m = -0.9\%$ (STO on LSAT) with $E_{ext} = 0$ is plotted in Fig. 12. The permittivity is suppressed for thinner films and its maximum is shifted towards higher temperatures, displaying similar trends for both ϵ and T_{max} as for BST on SRO in Sec IV A. T_{max} increases with decreasing l , but develops a peak at $l = 60$ nm and is again suppressed for very thin films due to depolarization effects. The screening length of LSAT is comparable to l_e for SRO, and thus so is l^* . The magnitude of ϵ is also comparable to that in BST films in Fig. 5; it results from similar values of the Landau coefficients and the value of the compressive strain in both films (see Table I). To our knowledge, there exists only one published dielectric measurement on strained STO with the polarization normal to the film-substrate interface; this experiment, performed on a $l = 50$ nm STO film grown on LSAT ($u_m = -0.9\%$)⁶ yields $\epsilon_{max}^{exp} \approx 400$, that is in a good agreement with our calculated maximum value of permittivity, $\epsilon_{max}^{calc} = 364$ for this film/substrate combination. We investigate the effect of compressive strain on the relative permittivity in Fig. 13. We observe that increased compressive strain shifts the permittivity curve towards higher temperatures and larger shifts of T_{max} occur for thinner films.

We display the nonswitchable polarization as a function of film thickness and misfit strain at $T = 300$ K and $E_{ext} = 0$ in Fig. 14. Again, the polarization shows similar behavior as in BST films in Sec. IV A; it decreases with increasing film thickness and is suppressed for very thin films (< 50 nm) due to depolarization effects. Increasing the strain results in higher polarization, in agreement with Fig. 10; this time however the polarization values change due to the effect of a nonzero bias field. In the inset, the temperature-dependence of the nonswitchable polarization is plotted in $l = 100$ and $l = 500$ nm STO films at misfit strain $u_m = -0.9\%$ (STO on LSAT substrate). The polarization decreases with increasing temperature.

Unstrained bulk STO remains paraelectric down to zero temperature. However, as previously noted, a ferroelectric regime occurs for strained STO films.⁶ We plot the transition temperature T_{ferro} , separating switchable and nonswitchable polarization regimes, as a function of film thickness and misfit strain with $E_{ext} = 0$ in Fig. 15. We predict a ferroelectric phase to occur for compressive strains larger than 2.0%, and note that ferroelectricity is recovered here for the thinnest STO films, as one goes from a thick-film nonswitchable regime to a thin-film switchable one (at fixed T); e.g. ferroelectricity emerges at -2.0% strained films for thicknesses, $30 \lesssim l \lesssim 160$ nm. This is distinct from the behavior previously described in BST films, where ferroelectricity is lost by making films thinner (see Fig. 4). T_{ferro} indicates a maximum at $l^* \approx 60$ nm, and this peak is due to depolarization effects (see Eq. 4) that reduce the transition temperature to zero for the thinnest films. T_{ferro} decreases in thicker films ($l > 60$ nm) for values of compressive strain $u_m > 2.0\%$.

Inhomogeneous Strain Model

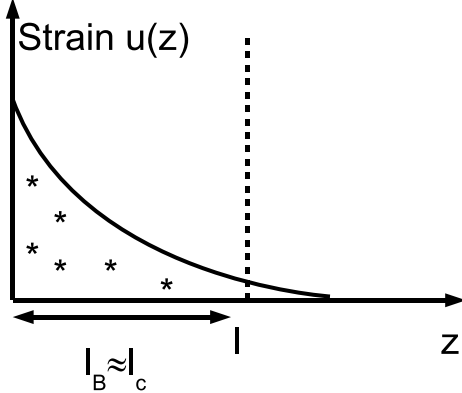


Figure 16: Schematic of the inhomogeneous strain model⁹ where the effective bias field $W(z)$ is spatially-dependent due to flexoelectric coupling; here the characteristic length-scales associated with the strain relaxation (l_c) and the buffer layer (l_B), where the elastic defects reside, are assumed comparable with the overall film thickness (l).

as shown in Fig. 15. However, it increases with increasing film thickness for small values of compressive strain ($u_m \lesssim 1.5\%$), similarly to BST films on SRO substrates (with $u_m = -0.5\%$) in Fig. 4. We note here that although T_{ferro} increases, it has negative nonphysical value for these low strain values, and thin films remain in the nonswitchable regime down to zero temperature. As noted previously, the thickness-dependence of this temperature scale arises from competition between strain and bias field contributions (see Eq. 14); the former dominates for large enough mismatch strains ($u_m \gtrsim 2.0\%$), and in this case T_{ferro} decreases with increasing film thickness.

V. DISCUSSION

Next we explore the implications of our results and the origin of our model assumptions. We begin with a general discussion of the effective bias field in epitaxial perovskite oxide films. Both the inhomogeneous (see Fig. 16) and the segregated (see Fig. 3) strain models describe the thickness-dependent dielectric properties of ferroelectric films consistently with experiment, and thus further measurements are required to determine the presence/absence of underlying inhomogeneous strain throughout the film. These models each have effective bias fields, one that is spatially varying⁹ and the other that is uniform, and it is exactly this feature that we exploit in a proposed benchtop experiment to distinguish these two scenarios.

An effective bias field breaks up-down symmetry at all temperatures. In a film above the zero-(external) field ($E_{ext} = 0$) ferroelectric transition temperature T_{ferro} , this results in a nonzero macroscopic polarization in zero

external electric field (see Eq. 10); for the sake of completeness, we note that the Curie temperature T_c^* refers to the paraelectric-ferroelectric transition at zero total field ($E_l^T \equiv W_l + E_{ext} = 0$). While this polarization can vary with temperature, making the film pyroelectric, it should not be confused with a ferroelectric spontaneous polarization. The correct distinction between polar and ferroelectric films is made on the basis of switchability, as determined, for example, through a hysteresis measurement. In a nonswitchable polar film, there is only one locally stable polarization state with $E_{ext} = 0$, and the system will show dielectric behavior in a finite external electric field. On the other hand, if there are two (or more) stable polarization states for the system with $E_{ext} = 0$ that can be switched by application of an external electric field, then the film is ferroelectric, and it will exhibit a characteristic ferroelectric hysteresis loop. An effective bias field W_l will lead to a lateral shift in the ferroelectric hysteresis loop, which can be used to determine the associated effective bias voltage across the film. Field offsets have been indeed experimentally observed in 100 nm $PbZr_{0.2}Ti_{0.8}O_3$ (PZT) thin films.³⁹ We also remark that an effective bias field will make the two polarization states symmetry-inequivalent with different energies.

The transition from nonswitchable to switchable ferroelectric phases usually occurs as a function of decreasing temperature at T_{ferro} . The detailed thickness-dependence of T_{ferro} depends on material-specific parameters, as can be seen in Figs. 4 and 15 for BST and STO thin films. More generally the l -dependence of the dielectric properties enters via the strain relaxation (Eq. 1), the bias (Eq. 2) and the depolarization fields. For the strain relaxation, an exponential decay on a characteristic length scale of several hundred nanometers was observed experimentally.^{23,27} In our model, we assume the same exponential decay for the magnitude of the uniform effective bias field. These two quantities determine the thickness-dependence of the quantities of interest in all but the very thinnest films, where the depolarization field term dominates, strongly suppressing T_{ferro} , the polarization, and T_{max} . In the case of the temperature T_{ferro} (see Figs. 4 and 15), the strain and effective bias contributions oppose each other (Eq. 14) and depending on their relative strengths, $T_{ferro}(l)$ increases (BST case where W_l dominates) or decreases (situation for strained STO where u_l is greater) with increasing film thickness l .

A direct consequence of the strain contribution to T_{ferro} is that we predict that ferroelectricity can be strengthened as the films get thinner (u_l increases with decreasing l), resulting in a transition from a nonswitchable polar phase to a ferroelectric state below a critical thickness l_{CT} ; more specifically, for STO measured at 100 K and compressive strain -2.5% (see Fig. 15), the critical thickness below which ferroelectricity appears is $l_{CT} = 200$ nm. This runs counter to the usual notion that ferroelectricity is suppressed as the film thickness decreases, disappearing below a critical thickness; we note

that would be the case for BST on SRO (here W_l dominates the expression for T_{ferro}) where our results displayed in Fig. 4 indicate a critical thickness of about 100 nm at temperature 60 K. This reentrant ferroelectricity as a function of decreasing l should be readily observable in an appropriate experiment for strained STO films with the polarization normal to the film-substrate interface.

Both the strain and the effective bias contributions act to decrease $T_{max}(l)$ and P_l (related by Eq. 9) as a function of increasing film thickness (l) (see Figs. 4, 7 and 14). By contrast, the depolarization contribution suppresses $T_{max}(l)$ and P_l with decreasing l . The dominance of this depolarization term explains the observed shift of the peak of $T_{max}(l)$ to higher values of l^* for semiconducting substrates (e.g. PSS) (see Fig 6) that have longer screening lengths (l_e) than their metallic counterparts (e.g. SRO); here we recall that the depolarization contribution to the free energy expansion is $\alpha_d \sim l_e/l$ (Eq. 4). We note that the thickness-dependent effect of the depolarization field on the relative permittivity has been noted before¹⁰ with a similar term, $\alpha_d^{BL} = a/l$, where boundary conditions for the spatially-varied polarization are proposed that incorporate the effects of a symmetry-breaking effective field. In this previous approach,¹⁰ a then is a boundary-related characteristic length. Since the thickness-dependence in both treatments is the same, one obtains similar results for the relative permittivity with appropriate choice of these length-scales (l_e and a) although their physical origins are different. Here we have extended this treatment to address the thickness-dependence of other dielectric properties (e.g. polarization) as well, and we note that the previous inhomogeneous strain approach⁹ did not include such depolarization effects for thin ferroelectric films.

The smearing of the sharp peak in the temperature-dependent dielectric response(Figs. 5, 6 and 12) in zero electrical field ($E_{ext} = 0$) is a signature of the presence of a finite effective bias field W ; this point has been much discussed previously both here (see Eqs. 8, 10) and by others.^{9,10,19,25} W_l assumes larger values for thinner films (see Eq. 2) and so pushes the permittivity to smaller values in thinner films (see Eq. 8), in accordance with experiment (Fig. 1). In the bulk limit, both the strain and the bias field vanish and bulk behavior of the dielectric properties is recovered.

While there is general agreement that effective bias fields play an important role in the properties of perovskite thin films,^{9,10,19,25} their specific origins and their spatial natures in the films are less well understood. For example, an effective bias field can be produced by a spatially (z)-dependent strain via a flexoelectric effect;⁹ we will refer to this as the inhomogeneous strain model and it is schematically depicted in Fig. 16. In this scenario, misfit dislocations are distributed roughly isotropically throughout the film and produce strain gradients. By contrast, in the segregated strain model presented here, the elastic defects are concentrated in a thin buffer layer near the film-substrate interface (see Fig. 2 and Fig. 3).

Benchtop Probe for the Segregated Strain Model

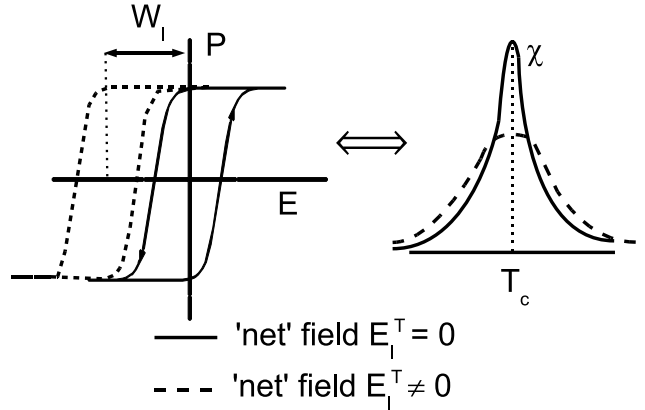


Figure 17: Schematic of a benchtop probe to test for the segregated strain model: the field offset (W_l) in the observed hysteresis loop can be tuned to zero by application of an electric field $E_{ext}^*(l) = -W_l$; in this case, the relative permittivity sharpens since the net (thickness-dependent) field $E_l^T = E_{ext}^*(l) + W_l = 0$.

This buffer layer itself breaks the up-down symmetry of the film, which then results in a nonzero effective field. To be more specific, it may be that an edge dislocation in the buffer layer produces a local polar distortion. This makes the buffer layer polar and produces a field in the uniform film. We then expect the strength of the effective bias field to be related to the areal density of dislocations, and thus to the magnitude of the homogeneous strain in the film.

As we have shown in Sec. IV A, using the segregated strain model (see Figs 2 and 3) we recover the thickness-dependent dielectric properties of BST films consistent with those measured²³ and calculated using flexoelectric effects⁹ within an inhomogeneous strain scenario (see Fig 16). Therefore, in order to determine which of these two models is applicable to a particular film, additional experimental characterization is necessary. The presence of strain gradients in the BST films studied using flexoelectricity⁹ was verified by x-ray analyses⁴⁰, though similar studies on different BST films (on different substrates) indicate the absence of such inhomogeneous strain.⁴¹ Therefore it is clear that observations of thickness-dependent permittivities and polarizations are not enough to indicate the underlying strain profile of the ferroelectric film. Naturally the presence/absence of strain gradients can be addressed directly by x-ray diffraction but this probe may not be always easily accessible or practical.

Here we emphasize that the effective bias fields associated with these two strain models are spatially different (see Figs 16 and 3), and we will use this distinction to propose a benchtop experiment to distinguish between these two scenarios. In the inhomogeneous strain model,⁹ the

effective bias field is spatially nonuniform; more specifically is proportional to the strain gradient via a flexoelectric coupling, and thus has an exponentially decaying spatial profile within the film (see Fig 16). By contrast, in the segregated strain model (see Fig 3), the effective bias field is uniform from the edge of the buffer layer to the surface. Assuming that this effective bias field W_l is uniform in the majority of the film, one can tune an external electric field to the right value, $E_{ext}^*(l) = -W_l$, to create a net zero-field condition ($E_T(l) = E_{ext}^*(l) + W_l$) where the specific value of the necessary external field would be thickness-dependent. Therefore there would exist an external field value $E_{ext}^*(l)$ when the hysteresis loop would no longer have a field offset; at this value of the applied external field, a sharp peak in the temperature-dependence of the relative permittivity should be observed (Fig 17). We emphasize that this must be a unipolar hysteresis experiment, with single top and bottom electrodes; many measurements are performed across two top electrodes, namely two series capacitors, where one would always be uncompensated. Another probe of the spatial uniformity of W would be to measure T_{ferro} as a function of E_{ext} ; for a uniform effective bias field there would be a sharp peak in T_{ferro} , as shown in Fig. 8. This pronounced peak would not be present for a spatially-varying effective bias field $W(z)$ since the latter would have varying magnitude in the sample and no particular value of applied (uniform) E_{ext} could completely compensate for it everywhere in the film; physically we note that $W(z)$ could arise from coupling of the polarization to gradients in the strain,⁹ in chemical composition, and in temperature.^{10,42,43} There do exist graded ferroelectric structures where such spatially varying quantities are explicitly present by design; here a charge offset is often observed in the charge-voltage hysteresis loops,⁴² and this could serve as an indicator of underlying gradients in ferroelectric films if a suitable “charge origin” could be chosen as a reference.

We emphasize that we expect different films, with varying compositions, substrates and growth conditions, to have diverse strain and effective bias field profiles. The inhomogeneous scenario may describe some while others may be better modelled by the segregated strain approach; still others may exhibit intermediate behavior. By carefully monitoring growth conditions, it should be possible to control the density and spatial distribution of strain-relieving defects; in some case, it may even be feasible to kinetically inhibit them to obtain uniform coherently-strained films.⁶ We emphasize that in each case, the strain and effective bias field distributions must be carefully characterized for a full interpretation of the measured thickness-dependent dielectric behavior, and we have presented simple proposals for benchtop measurements to ascertain the importance of strain gradients in the films.

VI. SUMMARY

In conclusion, we have demonstrated that a segregated strain model (cf. Fig 2) describes the observed thickness-dependent dielectric properties of ferroelectric films as well as does a previous model of inhomogeneous strain.⁹ Therefore such thickness-dependent behavior is not signatory of underlying strain gradients, and more measurements must be performed to determine the strain profile in the film. If the effective bias field is spatially uniform, it can be compensated by the application of an applied external electric field $E_{ext}^*(l) = -W_l$ whose value will be dependent on the overall film thickness l . Benchtop experiments performed with $E_{ext} = E_{ext}^*(l)$ will yield bulk-like sharp dielectric responses. However such compensation will not be possible if the effective bias field is spatially varying, since then its effects cannot be cancelled by the application of an external uniform field.

We have compared our results with experiment (BST on SRO) whenever possible and have also made predictions for measurements on strained STO films with out-of-plane polarization. Agreement with existing ab-initio calculations, when appropriate, has been good. The possibility of reentrant ferroelectricity in strained STO films has also been discussed and we hope that this will be explored experimentally in the near future.

Our phenomenological study of planar films suggests that their thickness-dependent dielectric properties are not indicative of underlying inhomogeneous strain, and are consistent with other strain profiles. We view this project as the beginning of a broader study of the physical consequences of boundary-induced effects in ferroelectrics of increasingly complex host topologies. A next step is to explore cases where the strain gradients will be induced by geometry: examples include curved films and cylindrical shells. Because of the coupling between the elastic and the electrical degrees of freedom in these systems, we expect tunable strain gradients to stabilize novel polarization configurations with rich phase behavior, and here flexoelectric effects should definitely be investigated. More complex host geometries and boundary conditions are expected to favor more novel orderings and dielectric properties; the possibility of identifying and characterizing these features in three-dimensional ferroelectrics on the nanoscale could also be useful in the design of future ferroelectric memories.⁴⁴

We thank G. Catalan, M. Dawber, D. Hamman, J. Junquera, V. Kiryukin, M. Pál, J. Scott, and D. Vanderbilt for discussions. We are grateful to I2CAM for support (LP) and to the Aspen Center for Physics for hospitality (PC, KMR). We also acknowledge support from grants NSF-DMR-0645461 (LP), NSF-NIRT-ECS-0608842 (PC) and NSF-DMR-0507146 (KMR).

¹ O. Auciello, J.F. Scott and R. Ramesh, *Physics Today* **51**, 22 (1998).

² J.F. Scott, *Ferroelectric Memories* (Springer, Berlin, 2000).

³ M.E. Lines and A.M. Glass, *Principles and Applications of Ferroelectrics and Related Materials* (Clarendon Press, Oxford, 1977).

⁴ N.A. Pertsev, A.K. Tagantsev and N. Setter, *Phys. Rev. B* **80**, 1988 (1998).

⁵ K.J. Choi, M. Biegalski, Y.L. Li, A. Sharan, J. Schubert, R. Uecker, P. Reiche, Y.B. Chen, X.Q. Pan, V. Gopalan, L.-Q. Chen, D.G. Schlom and C.B. Eom, *Science* **306**, 1005 (2004).

⁶ J.H. Haeni, P. Irvin, W. Chang, R. Uecker, P. Reiche, Y.L. Li, S. Choudhury, W. Tian, M.E. Hawley, B. Craigo, A.K. Tagantsev, X.Q. Pan, S.K. Streiffer, L.Q. Chen, S.W. Kirkchoefer, J. Levy and D.G. Schlom, *Nature* **430**, 758 (2004).

⁷ D. Balzar, P.A. Ramakrishnan and A.M. Hermann, *Phys. Rev. B* **70**, 092103 (2004).

⁸ S.P. Alpay, I.B. Misirlioglu, V. Nagarajan and R. Ramesh, *Appl. Phys. Lett.* **85** 2044 (2004); V. Nagarajan, C.L. Jia, H. Kohlstedt, R. Waser, I.B. Misirlioglu, S.P. Alpay and R. Ramesh, *Appl. Phys. Lett.* **86** 192910 (2005).

⁹ G. Catalan, L.J. Sinnamon and J.M. Gregg, *J. Phys. Condens. Mat.* **16**, 2253 (2004); G. Catalan, B. Noheda, J. McAneney, L.J. Sinnamon and J.M. Gregg, *Phys. Rev. B* **72**, 020102 (2005).

¹⁰ A.M. Bratkovsky and A.P. Levanyuk, *Phys. Rev. Lett.* **94**, 107601 (2005).

¹¹ M. Dawber, K.M. Rabe and J.F. Scott, *Rev. Mod. Phys.* **77**, 1083 (2005).

¹² T. Suzuki, Y. Nishi and M. Fujimoto *Philos. Mag. A* **79** 2461 (1999).

¹³ H.P. Sun, W. Tian, X.Q. Pan, J.H. Hanei and D.G. Schlom, *Appl. Phys. Lett.* **84** 3298 (2004).

¹⁴ V. Nagarajan, C.L. Jia, H. Kohlstedt, R. Waser, I.B. Misirlioglu and S.P. Alpay, *Appl. Phys. Lett.* **86** 192910 (2005).

¹⁵ W. Ma and L.E. Cross, *Appl. Phys. Lett.* **78**, 2920 (2001); *ibid* **79**, 4420 (2001); *ibid* **81** 3440 (2002); *ibid* **82** 3293 (2003).

¹⁶ A. Gruverman, B.J. Rodriguez, A.I. Kingdon, R.J. Neimanich, A.K. Tagantsev, J.S. Cross and M. Tsukada, *Appl. Phys. Lett.* **83**, 728 (2003).

¹⁷ A.K. Tagantsev, *Sov. Phys. JETP* **61** 1246 (1985); *Phys. Rev. B* **34** 5883 (1986).

¹⁸ J.S. Speck and W. Pompe, *J. Appl. Phys.* **76** 466 (1994).

¹⁹ O. Vendik and S.P. Zubko *J. Appl. Phys.* **88** 5343 (2000).

²⁰ C.H. Ahn, T. Tybell, L. Antognazza, K. Char, R.H. Hammond, M.R. Beasley, O. Fischer and J.-M. Triscone, *Science* **276**, 1100 (1997).

²¹ T.M. Shaw, Z. Suo, M. Huang, E. Liniger, R.B. Laibowitz and J.D. Baniecki, *Appl. Phys. Lett.* **75** 2129 (1999).

²² P. Paruch, T. Tybell and J.-M. Triscone, *Appl. Phys. Lett.* **79** 530 (2001).

²³ L.J. Sinnamon, R.M. Bowman and J.M. Gregg, *Appl. Phys. Lett.* **81**, 889 (2002).

²⁴ A. Lookman, R.M. Bowman, J.M. Gregg, J. Kut, S. Rios, M. Dawber, A. Ruediger and J.F. Scott, *J. Appl. Phys.* **96** 555 (2004).

²⁵ M.M. Saad, P. Baxter, R.M. Bowman, J.M. Gregg, F.D. Morrison and J.F. Scott, *J. Phys: Cond. Mat.* **16**, L451 (2004).

²⁶ P. Chandra and P.B. Littlewood, cond-mat/0609347, to be published in **Physics of Ferroelectrics: A Modern Perspective**, eds. K.M. Rabe, C. H. Ahn and J-M. Triscone (Springer, Berlin 2007).

²⁷ H.J. Kim, S. Oh and H.M. Jang, *Appl. Phys. Lett.* **75** 3195 (1999).

²⁸ K. Johnston, X. Huang, J.B. Neaton and K.M. Rabe, *Phys. Rev. B* **71** 100103 (2005).

²⁹ S. Rios, A. Ruedinger, A.Q. Jiang, J.F. Scott, H. Lu and Z. Chen, *J. Phys. Cond. Mat.* **15** L305 (2003).

³⁰ R.R. Mehta, B. Silverman and J.T. Jacobs, *J. Appl. Phys.* **44** 3379 (1973).

³¹ R. Kretschmer and K. Binder *Phys. Rev. B* **20** 1065 (1979).

³² M. Dawber, P. Chandra, P.B. Littlewood and J.F. Scott, *J. Phys. Cond. Mat.* **15** L393 (2003); P. Chandra, M. Dawber, P.B. Littlewood and J.F. Scott, *Ferroelectrics* **313**, 7 (2004).

³³ J. Junquera and Ph. Ghosez, *Nature* **422** 506 (2003).

³⁴ D.L. Tilley, *Ferroelectrics* **134**, 313 (1992); D.L. Tilley in *Ferroelectric Ceramics*, eds. N. Setter and E.L. Colla (Brikhauser Verlay, Basel 1993) pp. 163-184.

³⁵ A. Antons, J.B. Neaton, K. M. Rabe, and D. Vanderbilt *Phys. Rev. B* **71** 024102 (2005).

³⁶ C. Lichtensteiger, J.-M. Triscone, J. Junquera and P. Ghosez, *Phys. Rev. Lett.* **94** 047603 (2005).

³⁷ L.Q. Chen in **Physics of Ferroelectrics: A Modern Perspective**, eds. C. H. Ahn, K.M. Rabe and J-M. Triscone (Springer, Berlin 2007).

³⁸ D. Fuchs, C.W. Schneider, R. Schneider, and H. Rietschel *J. Appl. Phys.* **85** 7362 (1999).

³⁹ H.N. Lee, S. Nakhmanson, M.F. Chisholm, H.M. Christen, K.M. Rabe and D. Vanderbilt, *Fundamental Physics of Ferroelectrics* (2007).

⁴⁰ G. Catalan, B. Noheda, J. McAneney, L.J. Sinnamon and J.M. Gregg, *Phys. Rev. B* **72** 020102 (2005).

⁴¹ D. Balzar, P.A. Ramakrishnan, P. Spagnol, S. Mani, A.M. Hermann and M.A. Matin, *Jpn. J. Appl. Phys.* **41** 6628 (2002).

⁴² Z.-G. Ban, S.P. Alpay and J.V. Mantese, *Phys. Rev. B* **67**, 184104 (2003); Z.-G. Ban, S.P. Alpay and J.V. Mantese, *Integ. Ferr.* **58** 1281 (2003).

⁴³ S.P. Alpay, Z.-G. Ban and J.V. Mantese, *Appl. Phys. Lett.* **82** 1269 (2003).

⁴⁴ Y. Arimoto and H. Ishiara, *MRS Bulletin* **29** 823 (2004).